Biomaterials Science

Biodistribution and toxicological evaluation of micron- and nano-sized erythrocyte-derived optical particles in healthy Swiss Webster mice

Journal:	*Biomaterials Science*
Manuscript ID	BM-ART-11-2018-001448.R1
Article Type:	Paper
Date Submitted by the Author:	29-Jan-2019
Complete List of Authors:	Vankayala, Raviraj; University of California Riverside, Bioengineering Mac, Jenny; University of California, Riverside, Department of Biochemistry Burns, Joshua; University of California, Riverside, Bioengineering Dunn, Eugene; University of California, Davis, Comparative Pathology Laboratory Carroll, Stefanie; University of California, Davis, Comparative Pathology Laboratory Bahena, Edver; University of California Riverside, Bioengineering Patel, Dipti; University of California Riverside, Bioengineering Griffey, Stephen; University of California, Davis, Comparative Pathology Laboratory Anvari, Bahman; University of California Riverside, Bioengineering

Biomaterials Science

ARTICLE

Biodistribution and toxicological evaluation of micron- and nano-sized erythrocyte-derived optical particles in healthy Swiss Webster mice

Received 00th January 20xx,
Accepted 00th January 20xx

DOI: 10.1039/x0xx00000x

www.rsc.org/

Raviraj Vankayala,[a†] Jenny T. Mac,[b†] Joshua M. Burns,[a] Eugene Dunn,[c] Stefanie Carroll,[c] Edver M. Bahena,[a] Dipti K. Patel,[a] Stephen Griffey,[c] and Bahman Anvari[a,b*] († equally contributed)

Particle-based systems provide a capability for the delivery of imaging and/or therapeutic payloads. We have engineered constructs derived from erythrocytes, and doped with the FDA-approved near infrared dye, indocyanine green (ICG). We refer to these optical particles as NIR erythrocyte-mimicking transducers (NETs). A particular feature of NETs is that their diameters can be tuned from micron- to nano-scale. Herein, we investigated the effects of micron- (≈ 2.6 μm diameter), and nano- (≈ 145 nm diameter) sized NETs on their biodistribution, and evaluated their acute toxicity in healthy Swiss Webster mice. Following tail vein injection of free ICG and NETs, animals were euthanized at various time points up to 48 hours. Fluorescence analysis of blood showed that nearly 11% of the injected amount of nano-sized NETs (nNETs) remained in blood at 48 hours post-injection as compared to ≈ 5% for micron-sized NETs (μNETs). Similarly, at this time point, higher levels of nNETs were present in various organs including the lungs, liver, and spleen, indicating that nano-encapsulation of ICG in these constructs provided a method to prolong its circulation. Histological analyses of various organs, extracted at 24 hours post-injection of NETs, did not show pathological alterations. Serum biochemistry profiles, in general, did not show elevated levels of the various analyzed biomarkers associated with liver and kidney functions. Values of various hematological profiles remained within the normal ranges following the administration of μNETs and nNETs. Results of this study suggest that erythrocyte-derived particles can potentially provide a non-toxic platform for delivery of ICG.

Introduction

Particle-based systems play a prominent role in the field of clinical medicine as they provide a capability to deliver imaging or therapeutic agents to specific sites within the body.[1, 2] In relation to particles that deliver optical agents for imaging or phototherapeutic applications, the use of materials that are photo-activated by near infrared (NIR) excitation wavelengths (≈700–1300 nm) is especially advantageous since at this optically transparent window there is minimal light absorption by water and proteins, and diminished scattering by biological components, leading to increased depth of penetration on the order of a few centimeters.[3] Furthermore, given that there is negligible tissue autofluorescence over this spectral window, the use of exogenous fluorescent materials can enhance the image contrast.

One particular NIR exogenous dye is indocyanine green (ICG). It is a tricarbocyanine molecule with maximum spectral peak in the range of ≈ 780 – 810 nm, depending on the solvent and concentration.[4, 5] To date, ICG remains as the only NIR-activated agent approved by United States Food and Drug Administration for specific applications such as ophthalmic angiography, and assessment of liver and cardiovascular functions.[6] Additionally, considerable efforts have been devoted to utilize ICG as a photothermal therapy reagent and photosensitizer for photodynamic therapy.[7-10]

Despite its effective usage in clinical medicine, the major limitations of ICG are its short half-life within plasma (2~4 minutes), with nearly exclusive uptake by hepatocytes and elimination from the body through the hepatobiliary mechanism.[11, 12] Encapsulation of ICG has been used as a strategy to reduce its non-specific interactions with plasma biomolecules, and increase its circulation time.[13] Previously, we reported the encapsulation of ICG into a synthetic polymer, poly (allylamine) hydrochloride cross-linked to sodium phosphate.[14] When coated with 5 kDa poly (ethylene) glycol, these ICG-containing nanoparticles with peak diameter of ≈ 80 nm remained detectable within the circulation at 90 minutes post intravenous injection in mice.

Apart from synthetic polymers,[14, 15] and liposomes [16] attention has been given to the use of mammalian cells as

[a] Department of Bioengineering, University of California, Riverside, 900 University Avenue, Riverside CA 92521, USA. Email: anvarib@ucr.edu
[b] Department of Biochemistry, University of California, Riverside, 900 University Avenue, Riverside CA 92521, USA
[c] Comparative Pathology Laboratory, School of Veterinary Medicine, University of California, Davis, Sacramento, CA 95616, USA
† Electronic Supplementary Information (ESI) available: [details of any supplementary information available should be included here]. See DOI: 10.1039/x0xx00000x

carriers for delivery of imaging/contrast reagents or therapeutic payloads.[16, 17] We previously provided the first report on the engineering of erythrocyte-derived nano-sized vesicles loaded with ICG, and their utility for fluorescence imaging and photo-destruction of human mammalian cells.[18] We refer to these constructs as NETs (NIR erythrocyte-derived transducers) as they can convert the absorbed NIR light to emit fluorescence, generate heat, or induce photochemistry.[19]

Recently, other investigators have encapsulated ICG or other agents such as gold nanoparticle and doxorubicin into erythrocytes-derived nano-constructs.[20-24] For example, nano-constructs (≈ 80 nm diameter) composed of poly (lactic-co-glycolic acid) (PLGA) core fused with erythrocyte-derived membranes were retained in mice blood at two days post tail vein injection.[25] Piao et al have reported that gold nanocages cloaked with erythrocyte membranes (≈ 90 nm diameter) were present in mice blood 24 hours after tail vein injection.[23] Godfrin et al have demonstrated the half-life of L-asparaginase encapsulated into erythrocytes as ~28 days for treatment of acute lymphocytic leukemia.[26] Hence, constructs derived from erythrocytes may offer a promising approach for increased circulation time within the vasculature.

A particular feature of NETs is that their diameters can be tuned from nano- to micron-scale levels based on appropriate mechanical manipulation methods.[27] The nano-sized NETs (nNETs) have relevance to optical imaging and phototherapy of tumors since particles with diameters < ≈ 200 nm are effective for extravasation into tumors by the enhanced permeability and retention effect resulting from leaky tumor vasculature and impaired lymphatic drainage.[28, 29] Micron-sized NETs (μNETs) have relevance to phototherapy of vasculature. An example of abnormal vasculature is associated with cutaneous capillary malformations such as port wine stain lesions where NETs can potentially serve as the target of laser irradiation to induce photo-destruction of the abnormal vasculature plexus.[30] To the best of our knowledge, there have not been prior studies to investigate the effects of the diameter of erythrocyte-derived constructs such as NETs on their resulting circulation kinetics. Additionally, we investigate the effects of NETs diameter on toxicology profiles of these particles in healthy mice. Results of this study provide important information not only towards identifying the window of time over which NETs-based optical imaging or phototherapy can be performed, but may also be useful for investigators interested in various optical sensing, imaging, or photo-therapeutic applications of erythrocyte-derived platforms.

Experimental

Fabrication of μNETs and nNETs

A schematic of the NETs fabrication process is presented in Fig. 1. Erythrocytes were separated from bovine whole blood (Rockland Immunochemicals, Inc., Limerick, PA, USA) by centrifugation process. Approximately, 1 ml of bovine whole blood was taken in an eppendorf, and centrifuged for 10 minutes (1600×*g* at 4 °C). The supernatant containing the plasma and buffy coat were discarded, and the resulting packed

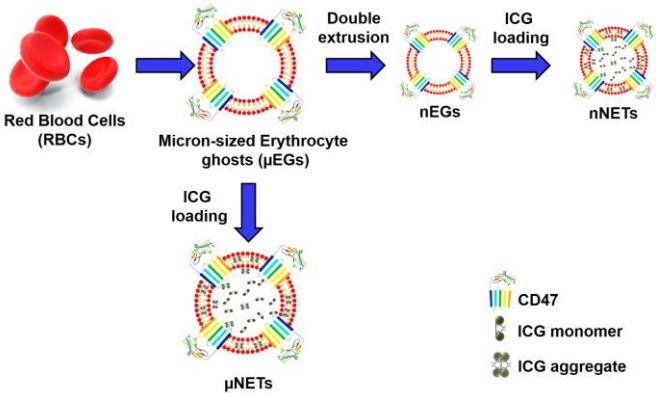

Fig. 1 Schematic representation for fabrication of μNETs and nNETs.

erythrocytes were washed twice with 310 mOsm, phosphate buffer solution (PBS) (referred to as the 1x solution) (Fisher Scientific, Hampton, NH, USA) at pH ~ 8.0. The erythrocytes were then subjected to sequential hypotonic treatment with 0.5× (155 mOsm, pH ~ 8.0) and 0.25× (80 mOsm, pH ~ 8.0) PBS, respectively. The centrifugation process (20,000×*g*, 15 minutes, 4 °C) was repeated until all the hemoglobin was depleted, resulting in an opaque white pellet. The obtained pellet containing micron-sized erythrocyte ghosts (μEGs) were resuspended in 1 ml of 1x PBS. To obtain nano-sized erythrocyte ghosts (nEGs), μEGs were extruded 20 times through 400 nm polycarbonate porous membranes, followed by 20 more extrusions through 100 nm polycarbonate porous membranes using an extruder (Avanti mini extruder, Avanti Polar Lipids, Alabaster, AL, USA).

To load ICG (MP Biomedicals, Santa Ana, CA, USA) into micron/nano-sized EGs, 350 μl of μEGs or nEGs suspended in 1x PBS were incubated with 23 μl of ICG stock solution (645 μM), 350 μl of Sorenson's buffer (Na_2HPO_4/NaH_2PO_4, 140 mOsm, pH ~8.0) and 280 μl nanopure water for 5 minutes at 4 °C in the dark. Resulting concentration of ICG in this loading buffer was 15 μM. Suspension was then centrifuged and washed twice with 1x PBS at 20,000×*g* for 20 minutes at 4 °C, or 100,000×*g* for 60 minutes to form μNETs and nNETs, respectively. The resulting μNETs and nNETs formulations were then re-suspended in 1 ml of 1x cold PBS. We note that the use of 15 μM ICG in the loading buffer can result in production of μNETs and nNETs with near maximum values of spectrally-integrated fluorescence emission.[27]

Characterizations

Absorption spectra of free 15 μM ICG, μNETs and nNETs suspended in 1x PBS were obtained using a UV-visible spectrophotometer (Jasco-V670 UV-vis spectrophotometer, JASCO, Easton, MD, USA) with optical path length of 1 cm. Fluorescence emission spectra of NETs in response to 720 ± 2.5 nm excitation light, spectrally filtered from a 450 W xenon lamp, were recorded in the range of 735–900 nm using a fluorometer (Fluorolog-3 spectrofluorometer, Horiba Jobin Yvon, Edison, NJ, USA). We normalized the fluorescence emission spectra as:

$$\zeta(\lambda)=\frac{F(\lambda)}{1-10^{-A(\lambda_{ex})}} \qquad (1)$$

where A and F are the respective wavelength (λ)-dependent absorbance and intensity of the emitted fluorescence light, and λ_{ex} is the excitation wavelength. The hydrodynamic diameters and zeta potentials of µNETs and nNETs suspended in 1x PBS were measured by dynamic light scattering (DLS) (Zetasizer Nano ZS90, Malvern Instruments Ltd, Westborough, MA, USA). We fitted lognormal functions to the DLS-based estimates of NETs' hydrodynamic diameters.

We imaged the µNETs by confocal laser scanning microscopy (CLSM). Sample solution (~ 10 µl) was added to Poly-L-lysine coated glass slide, followed by placing a coverslip on the top of the glass slide, and then imaging it with a confocal microscope (ZEISS 510, Carl Zeiss AG, Oberkochen, Germany). We imaged the nNETs by scanning electron microscopy (SEM). nNETs were fixed with 2.5% glutaraldehyde (Sigma Aldrich, St. Louis, MO, USA) overnight. Subsequently, 10 µl of the nNETs solution was added to Poly-L-lysine coated slide and dried (Critical-point-dryer, Balzers CPD0202) for 30 minutes followed by sputter coating with platinum for 20 s, and then imaging with SEM (FEI NNS450).

Assessment of ICG leakage from µNETs and nNETs under physiological temperature

Approximately, 2 ml of µNETs and nNETs suspensions were transferred into various eppendorf tubes, and incubated at 37 °C in the dark. After specific incubation times (0, 2, 4, 6, 24 and 48 hours), the NETs suspensions were centrifuged, and the pellet was then resuspended in 1 ml of fresh 1x PBS. Subsequently, the absorption spectra of re-suspended pellet and supernatant were recorded and compared to those for day 0 to assess the ICG leakage from µNETs or nNETs. The percentage of ICG leakage (υ) in µNETs and nNETs as a function of time were calculated as:

$$\upsilon(\%) = \frac{A_{\text{supernatant}}}{(A_{\text{pellet}} + A_{\text{supernatant}})} * 100 \qquad (2)$$

where A_{pellet} and $A_{\text{supernatant}}$ are the absorbance values of the pellet and supernatant recorded at 804 nm for each specific time point. Results of these experiments are presented as Electronic Supplementary Information (Fig. S1).

Biodistribution experimental design

Female Swiss Webster mice (≈ 20–25 g; ≈ 8–10 weeks old) were procured from Taconic Biosciences (Rensselaer, NY, USA). All animal maintenance and procedures were performed in accordance with the Public Health Service Policy, U.S. Department of Agriculture (USDA), and American Veterinary Medical Association (AVMA). Animal studies were approved by the University of California, Riverside Institutional Animal Care and Use Committee (protocol A-20170038). Animals were anesthetized by inhalation of 2% isoflurane in oxygen. Free ICG, µNETs or nNETs were administered intravenously via tail-vein injection while the animal was anesthetized. The injection volume for all samples was ≈ 100 µl. Injected dosages of ICG in our experiments were estimated as ≈ 58, 26.16, 14.5 µg/kg weight of the mouse for free ICG, µNETs, and nNETs respectively. For example, the injection dosage of free ICG used was estimated as follows: based on the molecular weight of ICG (775 Da), injection concentration of 15 µM free ICG corresponds to ≈ 11.6 µg/ml. Given the injection volume of ≈ 0.1 ml into each mouse, and an average mouse weight of ≈ 20 g, dosage of free ICG administered into an animal was ≈ 0.058 µg/g (11.6 µg/ml × 0.1 ml)/20 g, or ≈ 58 µg/kg. Taking into account the respective loading efficiency of 15 µM ICG into µNETs and nNETs as ≈ 45% and 25%,[27] the administered dosage of ICG in µNETs and nNETs formulations were estimated as ≈ 26.16 µg/kg and 14.5 µg/kg, respectively. These injected dosages of ICG were much lower than the lethal dosage in 50% of animals (LD_{50}) of ~ 62 mg/kg in mice.[31] We also note that loading efficiency of ICG is not the only metric that constitutes the ideal preparation of NETs. Other important metrics are the relative fluorescence quantum yield of NETs and their total fluorescence emission over a spectral band of interest. As we have reported previously, concentration of ICG in the loading buffer, ICG loading efficiency, and NETs' fluorescence quantum yield and total emission are inter-related parameters.[27] Increased levels of the indicated optical metrics can be associated with lower values of ICG loading efficiency.[27]

Mice were euthanized with compressed CO_2 gas at various times (5 minutes, 45 minutes, 2, 6, 24, and 48 hours) following injection with free ICG, µNETs or nNETs. Three mice were used for 5 minutes, 45 minutes and 2 hours time points, whereas, five mice were used for 6, 24 and 48 hours time points for each of the imaging agents, giving a total of 72 animals for the biodistribution studies.

Fluorescence imaging and analysis of extracted organs

Following euthanasia, liver, spleen, kidney (single), stomach, intestine, heart and lungs (two) were extracted and imaged fluorescently in a luminescence dark box. Two light emitting diodes (LEDs) delivering excitation light in the range of 700 ± 30 nm were used for illumination. Fluorescence emission from the organs was captured using a charge-coupled device (CCD) camera (Pixis 1024B, Roper Scientific, Trenton, NJ, USA) equipped with a long pass filter transmitting wavelengths greater than 810 nm. Camera exposure time was set to 90 s. Acquired fluorescent images were analyzed using ImageJ software. Regions of interests (ROIs) were selected for each organ. The mean intensity ($\bar{I}$) values per gram of each organ acquired from a given ROI at different post-injection times were

$$\bar{I} = \frac{\sum_{k=1}^{n}\left(\frac{1}{m_k}\right)\sum_{j=1}^{p}\frac{I_j}{p}}{n} \qquad (3)$$

calculated as:

where p is the total number of pixels in the ROI, m is the mass of a given organ, n is the numbers of a given organ, and I_j is the pixel intensity at the j^{th} pixel of a given image.

Biodistribution analysis

Extracted organs were grinded using Omni Tissue Homogenizer (Omni International, Inc., Kennesaw, GA, USA), and then incubated in 4 ml of sodium dodecyl sulfate (SDS) (Sigma Aldrich, St. Louis, MO, USA) solution (5% w/v in water) for one

hour to lyse the cells causing the release of ICG. We also collected 300 µl of blood from the heart by cardiac puncture. The blood sample was mixed with 1 ml of SDS solution and incubated for 30 minutes. This approach would ensure that any ICG or NETs uptaken by blood cells would also be released. Lysed organs and blood samples were centrifuged in the SDS solution at 16,000×g for one hour at 10 °C. Then the supernatants of the blood samples and homogenized organs were collected, and the corresponding fluorescence emission spectra in response to 720 ± 2.5 nm excitation wavelength were recorded using the fluorometer. ICG concentration in each organ was estimated by comparing the integrated fluorescence emission signal over the 735–900 nm spectral band with a calibration curve that related the integrated fluorescence emission over the same wavelength range to various concentrations of ICG in SDS solution. Specifically, we present the percentage of ICG recovered from each organ with respect to the initial dose (ID) injected per gram of organ (%ID/g).

For blood samples, the calibration curve related the spectrally-integrated fluorescence emission over the same wavelength range to various concentrations of ICG and blood in SDS solution. The integrated fluorescence emission value of whole blood in SDS solution without free ICG or NETs was subtracted from the integrated fluorescence emission values obtained for blood samples containing free ICG or NETs. The fluorescence profiles of ICG extracted from SDS-treated organs closely resembled that of free ICG dissolved in SDS (data not shown). This result validated that the fluorescence of ICG extracted from the various organs was not degraded in the presence of 5% SDS, and that autofluorescence was not a contributor to fluorescence emission at 720 ± 2.5 nm excitation wavelength.

Hematological, enzymatic, and histological evaluations

We injected ≈100 µl of µNETs or nNETs solutions via the tail-vein into anesthetized mice. At 24 hours post-injection, mice were euthanized, and blood samples were collected for serum biochemistry and enzymatic evaluations. This included three assays of hepatic function (Alanine Aminotransferase (ALT), Aspartate Aminotransferase (AST) and Alkaline Phosphatase (ALP)), and two renal assays (Urea nitrogen and creatinine) performed by a blood biochemical autoanalyzer (Roche Integra 400 Plus, Roche, Basel, Switzerland). A complete blood count (CBC) was also performed, which included white blood cells (WBCs) count, red blood cells (RBCs) count, mean corpuscular volume (MCV), hemoglobin, hematocrit, and platelets performed by a blood count analyzer (Drew HemaVet 950 FS, Drew Scientific, Miami Lakes, FL, USA).

A complete necropsy was performed and major organs including heart, liver, spleen, lungs and kidneys were collected. Tissues were fixed in 10% neutral buffered formalin (Fisher Scientific, Waltham, MA, USA), processed routinely into paraffin blocks and sectioned at 4 µm. These sections were stained with hematoxylin and eosin (H&E), and examined histologically for toxicity changes including thrombosis, inflammation, and necrosis. Ten mice were used for each agent for CBC and serum biochemistry, giving a total of 30 animals. Out of these, five mice were used for each agent for histological evaluations.

Statistical analysis

Statistical analyses were conducted using the Graphpad Instat 3.0 software by the one-way ANOVA analysis. We defined statistically significant differences at $*p < 0.05$.

Results and Discussion

Characterizations

Based on the analysis of CLSM images (Fig. 2A), average diameter of µNETs was ~ 3 µm. The SEM image of nNETs demonstrated the nano-sized dimensions of these NETs (Fig. 2B). The estimated mean peak values of hydrodynamic diameters for µNETs and nNETs, as estimated by the DLS method were 2.6 µm and 145 nm, respectively (Figs. 2C and 2D).

The mean ± standard deviation (SD) zeta-potential values for red blood cells (RBCs), µEGs, nEGs, µNETs and nNETs formulations in 1x PBS (pH ~ 7.4) were -11.03 ± 1.91 mV, -10.2 ± 1.93 mV, -9.96 ± 1.74 mV, -10.7 ± 1.42 mV and -11.4 ± 1.13 mV, respectively (Fig. 2E). Statistical analysis showed that the mean values of these zeta-potentials were not significantly different from each other. The similar zeta-potential values of µEGs, nEGs, µNETs and nNETs suggest that the sulfonate

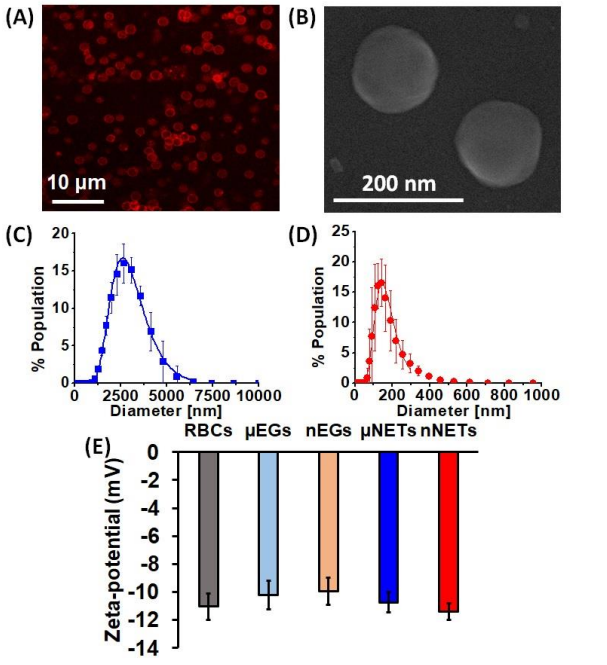

Fig.2 (A) Confocal laser scanning microscopy image of µNETs. A 633 nm laser was used for photo-excitation and a long-pass filter transmitting λ > 650 nm was used to collect the emitted NIR fluorescent light, falsely-colored in red. (B) Scanning electron microscopy (SEM) image for nNETs. Panels (C) and (D) represent the dynamic light scattering-based measurements of diameter distributions for µNETs and nNETs in 1x PBS, respectively. We present the mean of each measurement with errors bars representing standard deviations from the mean values. We fitted Lognormal functions to the measured diameter distributions. (E) Zeta-potentials for RBCs, µEGs, nEGs, µNETs and nNETs recorded in 1x PBS. Error bars represent the standard deviation for the three independent measurements.

portions of ICG molecules, which carry the negative charge of ICG, were not exposed to the extracellular environment, but rather localized within the membrane or within the interior core of NETs. The overall negative charge of erythrocyte-derived constructs can be attributed to the presence of the carboxylic groups of the sialic acid on erythrocytes membranes,[32-34] suggesting that these groups were preserved on both EGs and NETs.

The peak of the absorption spectrum for 15 µM free ICG dissolved in nanopure water was at 780 nm, and is associated with the monomeric form of ICG (Fig. 3A).[4] The absorption peak at 280 nm for µNETs and nNETs corresponds to the membrane proteins present on the surface of the NETs. The absorption spectra of µNETs and nNETs showed bathochromic (red) shifts in the monomeric peak of ICG from 780 nm to 804 nm, compared to free ICG.

We attribute this shift to encapsulation-induced changes in ICG including the formation of membrane protein-bound and phospholipid-bound forms with altered electronic states as compared to free form of ICG.[18, 27] Normalized fluorescence emission spectra of 15 µM free ICG, µNETs and nNETs in response to 720 nm excitation wavelength are presented in Fig. 3B. The respective spectral peak emission values for free ICG, µNETs and nNETs were at 793 nm, 809 nm, and 806 nm, corresponding to the monomeric forms of ICG.[4, 18]

Absorption spectra of µNETs and nNETs and supernatant after centrifugation at physiological temperature in dark over a period of 48 hours are shown in Figs. S1A and B. Using equation (2), we estimate the percentage leakage of ICG from µNETs and nNETs as ≈ 9.1% and 5.6%, respectively, at physiological temperature over time period of 48 hours (Fig. S1C).

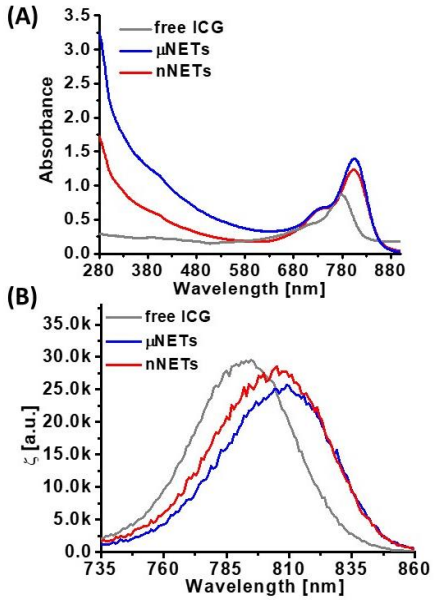

Fig. 3 Representative (A) Absorption and (B) normalized fluorescence emission spectra of 15 µM free ICG, µNETs, and nNETs. Both µNETs and nNETs were fabricated using 15 µM ICG in the loading buffer. Spectra for µNETs and nNETs were recorded in 1x PBS, and in nanopure water for free ICG. Prior to absorption and fluorescence spectral recordings, ICG and NETs solution were diluted by 50 and 10 times, respectively. Emission spectra were obtained in response to photo-excitation at 720 ± 2.5 nm.

Quantitative fluorescence imaging of extracted organs

Fluorescence emission from extracted liver was relatively weak at 6 hours post-injection of free ICG (Fig. 4A). This result suggests that by this time most of ICG was eliminated from the liver, its primary accumulation site. The weak fluorescence emission from the stomach could be due to the presence of chlorophyll (alfalfa) in the rodent diet,[35] or from the ICG eliminated from the liver and excreted into the intestine via bile.[36] At 24 and 48 hours post-injection, negligible fluorescence emission from the liver and intestines, and none from the remaining harvested organs were detected, suggesting that free ICG was eliminated from the body.

µNETs and nNETs showed higher fluorescence signals from the extracted liver, intestine, and stomach at 6 hours post-injection (Figs. 4B and C), suggesting a lower clearance rate of these particles from systemic circulation. Fluorescence emissions associated with µNETs and nNETs were detectable in liver up to 48 hours post-injection, suggesting that NETs had prolonged the availability of ICG within the body.

The mean fluorescence intensity ($\bar{I}$) values per gram of each extracted organ for free ICG, µNETs, and nNETs at 6, 24, and 48 hours post-injection time points are shown in Figs. 4D-F. When compared to free ICG and µNETs, nNETs showed statistically significant ($p < 0.05$) higher values of $\bar{I}$ in all extracted organs at 6 hours post-injection (Fig. 4D), indicating the higher accumulation of nNETs in these organs. At 24 hours post-injection, value of $\bar{I}$ associated with nNETs was significantly higher in spleen, lungs, intestine, heart and liver as compared to free ICG and µNETs (Fig. 4E).

At 48 hours post-injection, value of $\bar{I}$ associated with nNETs remained significantly higher in spleen, lungs, heart, and stomach than those for free ICG and µNETs (Fig. 4F). In contrast, there were no statistically significant differences between free ICG and µNETs at 48 hours in all organ samples.

Quantification of ICG content in blood

Fluorescence emission spectra of blood collected from healthy mice at 6 and 48 hours post-injection with µNETs and nNETs are presented in Fig. 5A. Fluorescence emission intensity of µNETs at 6 hours post-injection was higher than that at 48 hours post-injection over the spectral band 735–900nm, indicating that the fraction of these particles in the bloodstream was reduced between 6–48 hours. Nano-encapsulation improved the longevity of ICG in bloodstream as compared to micro-encapsulation as evidenced by higher fluorescence emission intensity of nNETs at 48 hours post-injection when compared to that of µNETs at 48 hours post-injection (Fig. 5A). Fluorescence emission spectrum of nNETs at 48 hours post-injection was comparable to that of µNETs at 6 hours post-injection.

We estimated the relative ICG content of blood at 5 min, 45 min, 2, 6, 24 and 48 h post-injection of free ICG, µNETs and nNETs formulations (Fig. 5B). nNETs showed higher levels of retention in blood than µNETs. Specifically, the relative ICG content of blood at 6 hours post-injection for nNETs was ≈ 21.6% as compared ≈ 12.5% for µNETs. At 48 hours post-injection, the relative amounts of ICG for nNETs and µNETs were

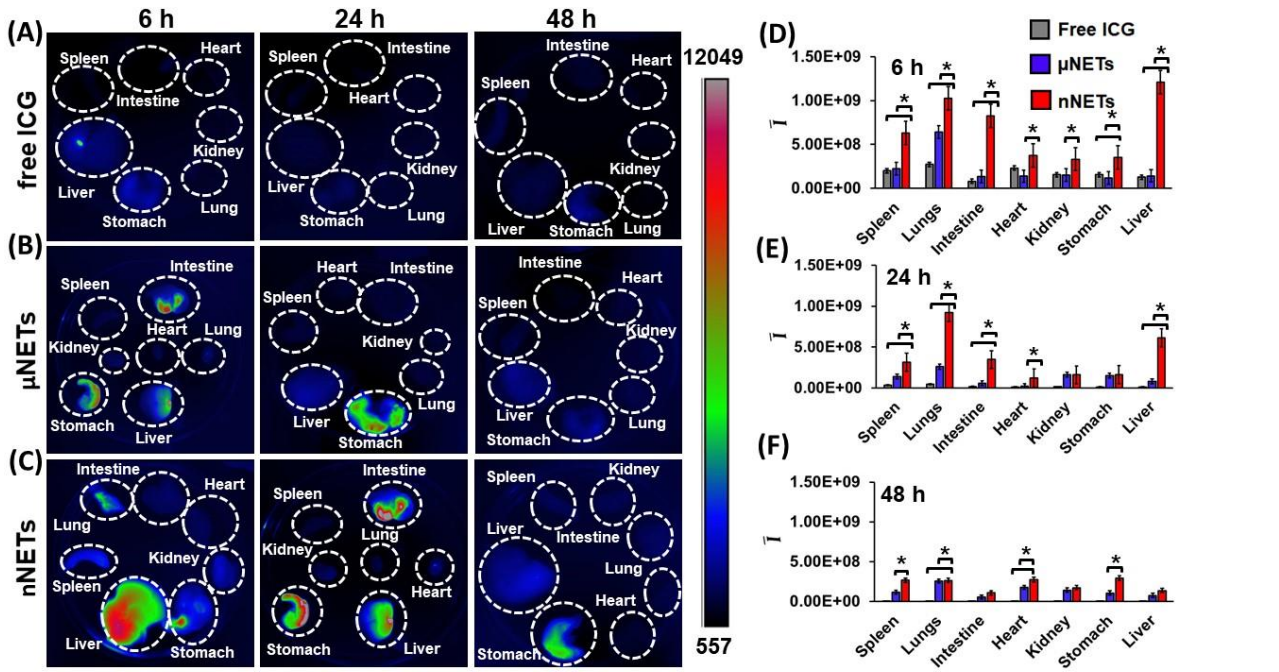

Fig. 4 Fluorescence images of organs extracted from healthy mice at 6, 24 and 48 hours post tail-vein injection with (A) indocyanine green (ICG) (15 μM), (B) μNETs, and (C) nNETs. Scale bar on the right (in arbitrary units) corresponds to fluorescence emission intensity. (D-F) Mean ROI fluorescence intensities per gram of extracted organ (see equation 3) from healthy mice at (D) 6, (E) 24, and (F) 48 hours post tail-vein injection of ICG (15 μM), μNETs and nNETs. Error bars represent standard deviation and the single asterisks denote statistically significant differences ($p < 0.05$) between the indicated pairs.

≈ 11.3% and 5.3%, respectively. The lower circulation time of μNETs as compared to nNETs can result from the increased uptake of μNETs in circulation by the mononuclear phagocytic system (MPS) that include the spleen and liver macrophages.

Biodistribution profiles

We quantified the relative amounts of free ICG, μNETs and nNETs in various organs at 6, 24 and 48 hours post-injections after homogenizing the organs (Fig. 6). In all organs, there were significantly greater levels of nNETs than μNETs and free ICG at 48 hours post-injection ($p < 0.05$). For example, at 48 hours post-injection, ≈ 18.8%, 12.8%, and 8% ID/g of nNETs, μNETs, and free ICG were present in the heart, respectively (Fig. 6A).

Lungs were another organ site for significantly higher accumulation of nNETs (Fig. 6B). The higher accumulation level of the nNETs in the lungs can be attributed due to their effective entrapment in the pulmonary capillaries. It is believed that endocytosis process by endothelial cells of the lungs capillaries is more effective in internalization of nano-sized particles as compared with micron-sized particles.[13, 37] At 48 hours post-injection time point, as compared to μNETs and free ICG, statistically significantly higher levels of nNETs were also detected in kidney (≈ 15% ID/g) and intestine (9% ID/g) (Figs. 6C and D).

At 48 hours post-injection, there were ≈ 27% and 15% ID/g of nNETs in spleen and liver, respectively. In contrast, at this time point, there were only about ≈ 18% and 3.6% ID/g of μNETs, and ≈ 9% and 3% ID/g of free ICG in spleen and liver, respectively (Figs. 6E and F). A higher level of nNETs in spleen at 48 hours post-injection suggests that nNETs were still within the circulation and passing through the spleen.

In addition to filtering foreign body materials, spleen is also involved in removal of and damaged or aged erythrocytes from the blood.[38] In the open blood circulation system of spleen, the arterial blood arrives into cords in the red pulp, which contain the splenic macrophages. Blood from the cords enters the venous sinuses of the red pulp through interendothelial slits with an average width of ≈ 650 nm.[39, 40] Due to their smaller diameters, nNETs (~ 145 nm mean peak diameter) can pass through these slits, and gain re-entry into the circulatory system. Some fraction of nNETs may also be uptaken by splenic macrophages of the red pulp located in the cords.

The circulation time of red blood cells (RBCs) depends on various biochemical and physical characteristics. For example, the presence of key membrane glycoproteins such as CD47, decay-accelerating factor (DAF), CD59, and CR1 on the RBC surface can impede phagocytosis and prolong the circulation time of RBCs.[41-44] Our previous results indicate that CD47 remains on the surface of μEGs and nNETs, suggesting that CD47 can survive the mechanical extrusion of μEGs,[45] and contribute to the extended circulation time of NETs by keeping them shielded from phagocytosis.

In addition to the presence of appropriate biochemical markers, healthy RBCs also have appropriate mechanical properties that allow them to deform and pass through the splenic slits. In contrast, senescent RBCs have reduced deformability.[46, 47] For example, nearly 35% increase in membrane surface viscosity is reported for aged RBCs as compared to young cells.[48] A reduction in deformability of senescent RBCs impairs their capability to pass through interendothelial slits. Aged RBCs are eventually phagocytosed by the red pulp macrophages,[39] and eliminated from circulation.

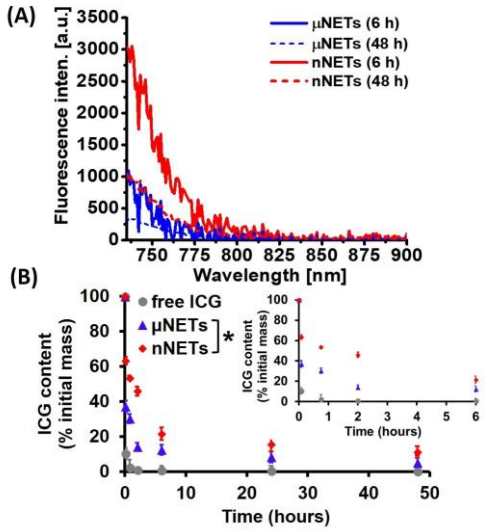

Fig. 5 (A) Fluorescence emission spectra of blood collected from healthy mice at 6 and 48 hours post tail-vein injection with μNETs and nNETs (λ_{ex} = 720 ± 2.5 nm) after baseline subtraction of blood emission spectra in SDS. (B) Estimated percentages of ICG recovered from mice blood after tail vein injection of ICG (circles ●), μNETs (triangles ▲) and nNETs (diamonds ◆) as a function of time. The inset represents the estimated percentages of ICG recovered from mice blood for the three agents at 0 min, 5 min, 45 min, 2 and 6 hours respectively. Error bars represent standard deviations, and the single asterisk denotes statistically significant differences ($p < 0.05$) between the indicated pairs for all the time points.

Similarly, μNETs (~ 2.6 μm mean peak diameter) may have reduced deformability to allow them to squeeze through splenic slits. This reduced deformability may be partially due to loss of hemoglobin during the fabrication process of NETs. Nash and Meiselman have reported that fresh micron-sized EGs with average reduction of approximately 125 times in cellular hemoglobin content had nearly 68% increase in average elastic shear modulus as compared to young intact RBCs.[48] With compromised mechanical integrity, specifically due to lowered deformability, μNETs are likely to remain within the cords and ultimately phagocytosed by the splenic macrophages. Combined with slowed blood flow rate in spleen,[40] resident red pulp macrophages can efficiently recognize μNETs and remove them from circulation. Changes in the deformability of NETs, as compared to RBCs, can also arise from alterations in membrane integral proteins such as the sialic acid-rich glycophorin A and B and 3 to affect their interactions with the membrane lipids and major cytoskeletal proteins, spectrin, actin and ankyrin, as well as alterations in cytoskeletal cross-linking itself.[49, 50]

Liver is another site for the elimination of foreign agents. Blood from both hepatic artery and portal vein are mixed together in the hepatic sinusoids before draining out of the liver to the heart through the central vein. Endothelial cells in liver sinusoids form a fenestrated lining containing pores with diameter of ≈ 170 nm,[51] which allow for passage of blood plasma to interact with hepatocytes.[52] A fraction of nNETs with diameters less than the pores' diameter are likely to leave the sinusoids and extravasate into the space of Disse where they can go undergo endocytosis by hepatocytes, and subsequently, secreted into the bile ducts, passaged into duodenum, and finally eliminated from the body. This mechanism of nNETs elimination is consistent with the hepatobiliary clearance of nanoparticles with diameters in the range of 150-200 nm,[52] and resembles hepatocytes-mediated elimination of liposomes and lipid-coated PLGA nanoparticles with similar characteristics consisting of mean diameters in the range of ≈ 150-195 nm and average zeta potentials between ≈ -19 to -10.6 mV.[53-55] Nanoerythrosomes with diameters <100 nm have also been reported to accumulate in hepatic parenchymal cells.[56]

In addition to hepatocytes, hepatic stellate cells located in the space of Disse between parenchymal and sinusoidal endothelial cells, can also uptake the nNETs extravasated out of the sinusoids. This mechanism of nanoparticles elimination has been reported for liposomes with average diameter of 92 nm and zeta potential of ≈ -20 mV.[57] The fraction of nNETs with diameters greater than the diameter of sinusoid pores, and μNETs can be uptaken by the Kupffer cells, macrophages adherent to the endothelial lining of the liver sinusoids.[52] This phagocytic uptake is consistent with the reported accumulation of nanoerythrosomes in Kupffer cells.[56]

A particular hydrodynamic phenomenon resulting from the high (≈ 50%) occupancy of blood volume by RBCs is the margination of particles to the vessels wall.[42] Under this phenomenon, RBCs avoid the micron-scale marginal layer of the blood that directly contacts the vessel wall and allow for other circulating particles to come in contact with the wall.[58, 59] It has been reported that 2 μm diameter hydrogel particles had enhanced margination when compared to their 500 nm diameters counterparts.[60] In relation to NETs, the margination phenomenon implies that μNETs may be in closer approximately to Kupffer and endothelial cells that line the sinusoids, resulting in greater uptake of these particles as compared to nNETs. Ultimately, degradation of μNETs by the

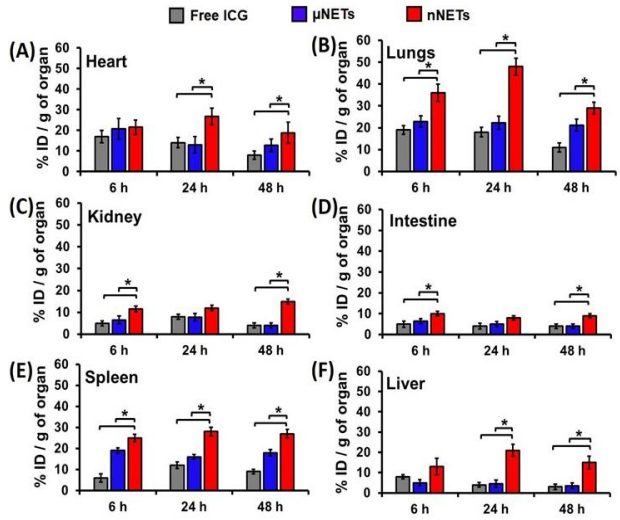

Fig. 6 Estimated percentage of ICG recovered from organs of mice with respect to the initial dose injected per gram of organ at 6, 24 and 48 hours post tail-vein injection with indocyanine green (ICG) (15 μM), μNETs and nNETs for (A) heart, (B) lungs, (C) kidney, (D) intestine, (E) spleen, and (F) liver. Error bars represent standard deviations, and the single asterisks denote statistically significant differences ($p < 0.05$) between the indicated pairs.

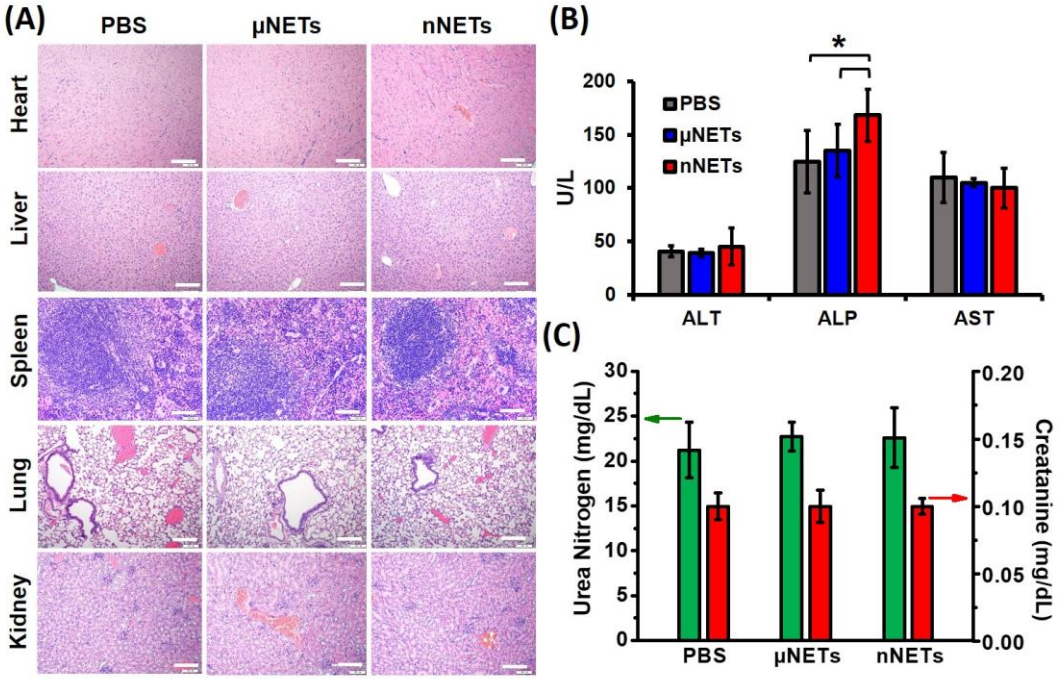

Fig. 7 (A) Representative H&E stained images of major organs collected from healthy mice at 24 hours post tail-vein injection with PBS, μNETs, and nNETs derived from bovine blood. Scale bars indicate 100 μm. (B) Levels of Alanine Aminotransferase (ALT), Aspartate Aminotransferase (AST) and Alkaline Phosphatase (ALP), associated with hepatic function. (C) Levels of Urea nitrogen and creatinine associated with renal function. Error bars represent standard deviations and the single asterisks denote statistically significant differences ($p < 0.05$) between the indicated pairs.

splenic and hepatic MPS can result in their reduced circulation time

Pathology, serum biochemistry and hematology

H&E stained sections of heart, liver, spleen, lung and kidney after 24 hours post intravenous injection of μNETs and nNETs were similar to PBS-injected (control) mice (Fig. 7A), indicating that NETs did not induce pathological alterations in these organs. The levels of blood biomarker enzymes (ALP, ALT, and AST) associated with the liver, and urea nitrogen and creatinine, associated with kidney functions are presented in Figs. 7B and C, respectively. Given that less than 20% of the injected dosages of NETs per gram of liver were detected at 48 hours (Fig. 6F), there may not be concerns with chronic toxicity to liver parenchyma that may otherwise arise as a result of prolonged retention of particles in liver. In contrast, nearly 53% of the injected dose of 20 nm diameter zinc oxide,[61] and 80% of 30 nm diameter superparamagnetic iron oxide nanoparticles[62] were retained in liver for at least 21 and 84 days, respectively.

Parameter	Normal Range	Free ICG	PBS	μNETs	nNETs
WBCs (K/μL)	3.0 – 14.2[63]	5.0 ±2.3[65]	10.2 ± 1.4	6.0 ± 1.3 *	9.0 ± 1.6 *
RBCs (K/μL)	5.0 – 9.5[63]	6.1 ±1.1[65]	8.9 ± 0.6	9.1 ± 1.0	9.0 ± 0.3
MCV (fL)	48.0 – 56.0[63]	57.2 ±1.9[65]	48.6 ± 5.1	48.6 ± 3.9	50.4 ± 5.4
Hemoglobin (g/dL)	10.9 – 16.3[63]	12.8 ± 2.2[65]	14 ± 0.7	12.8 ± 1.2	13.4 ± 0.6
Hematocrit (%)	41.5 – 48.2[64]	34.9 ±6.3[65]	43 ± 3.5	42.4 ± 5.0	43.5 ±3.1
Platelets (K/μL)	930 -1626[64]	721.2 ± 462.7[65]	1167 ± 155 *	1005 ± 145 *	1148 ± 193

Table 1 Hematology profiles of mice at 24 hours post tail vein injection of PBS (control), μNETs, and nNETs derived from bovine blood. Each experiment was repeated five times. Values represent the mean ± standard deviations. WBCs: white blood cells; RBCs: red blood cells; MCV: mean corpuscular volume. K denotes 1000. Single asterisks denote statistically significant differences of $p < 0.05$ between the indicated pairs. Reported ranges from reference 63 are based on values from various mouse strains, sex, and age. Reported ranges from reference 64 are for 16 weeks female Swiss Webster mice from Charles River Laboratories, Inc. Reported values from reference 65 are in response to 20 mg/kg of free ICG injection into Sprague-Dawley rats.

ALT and AST levels for μNETs and nNETs were similar to those for PBS-injected (control) mice (Fig. 7B). However, ALP levels were higher ($p < 0.05$) for nNETs when compared to those for PBS and μNETs. Levels of urea nitrogen and creatinine did not statistically differ as a function of the administered agent (Fig. 7C).

While the values for various hematological parameters can vary with the mouse strain, age, sex, and other factors, our measurements are within the normal ranges reported for these parameters,[63, 64] regardless of the administered agent (Table 1). Values of RBCs, MCV, hemoglobin and % hematocrit did not statistically differ as a function of the administered agent (Table 1). Despite our results that the levels of WBCs and platelets were significantly lower ($p < 0.05$) in response to administration of μNETs, as compared to those following the administration of PBS and nNETs, they were still within the normal ranges. Similarly, Marshall et al. have also reported a reduction in WBCs and platelets counts, but still within the normal range, upon injection of 20 mg/kg of free ICG into Sprague-Dawley rats

(Table 1), [65] a dosage substantially higher than our estimated dosages of 58 µg/kg for free ICG, and 26.16 and 14.5 µg/kg of ICG in µNETs and nNETs formulations, respectively.

Activation of Kupffer cells through interaction with NETs in the liver can induce the secretion of various cytokines for recruitment of circulating neutrophils to engulf NETs and become activated apoptotic cells. Kupffer cells then recognize and phagocytose apoptotic neutrophils expressing phosphatidylserine through P-selectin-medicated hepatic sequestration.[66] These endocytosed apoptotic cells are then degraded through phagosome maturation.[67, 68] This process results in elimination of neutrophils from circulation, corresponding to a decrease in WBCs count. Based on our results, this mechanism for elimination of neutrophils, which includes activation of Kupffer cells and interaction of neutrophils with NETs, appears to be more sensitive to µNETs as compared to nNETs.

Platelets interact with leukocytes in liver and spleen.[69] They bind to the hepatic sinusoidal endothelium in an integrin-dependent manner, leading to platelet and endothelial activation and leukocyte recruitment.[70] Activated platelets overexpress p-selectin glycoprotein ligand-1 (PSGL-1) can bind to leukocytes, neutrophils and monocytes resulting in platelet aggregation followed by the release of pro-inflammatory cytokines leading to clearance by the macrophages present in the complement system.[69, 71, 72] Our findings appear to suggest that the mechanisms leading to platelets activation, aggregation, and their ultimate clearance may have been more prone to µNETs as compared to nNETs. It is also possible that platelets aggregation and clumping, which may have been more prevalent in response to presence of µNETs, could have led to a decrease in the automated platelets count, as suggested in literature.[73] Finally, our findings are consistent with another study where noticeable signs of toxicity as determined by blood biochemical, hematological and histological assays were not observed in mice at 15 days post tail-vein injection of upconversion nanoparticles coated with RBC membranes.[22]

Conclusions

We have engineered erythrocyte-derived optical particles doped with ICG. The diameter of these constructs, referred to as NETs, can be adjusted from micron to nano scale. Nano-sized NETs were retained at higher levels in blood and various organs at 48 hours post tail vein injection as compared to free ICG and micron-sized NETs. Histological analyses of various organs, extracted at 24 hours post intravenous injection of NETs, did not show any pathological alterations. Serum biochemistry, in general, did not show elevated levels of the various analyzed biomarkers associated with liver and kidney functions. Values of various hematological profiles remained within the normal ranges following the administration of µNETs and nNETs. Results of this study suggest that erythrocyte-derived particles can potentially provide a non-toxic platform for delivery of payloads, and when constructed at nano-size scale, can extend the circulation time of their cargo. As optical platforms, NETs offer a great potential for clinical translation for light-based theranostic applications.

Conflicts of interest

Authors R.V. and B.A. have a financial interest in Radoptics LLC, which is pursuing the commercial development of the particles reported in this study. This interest did not interfere with the scientific work, judgement, and the objectivity of these authors with regards to the experimental procedures, data analysis, interpretation of results, reporting, and any other aspect of the study.

Acknowledgements

This study was supported in parts by grants from the National Institute of Arthritis and Musculoskeletal and Skin Diseases (1R01-AR068067-01A1), and the National Science Foundation (CBET-1509218). The electron microscopy images were obtained at the Central Facility for Advanced Microscopy and Microanalysis (CFAMM) at University of California, Riverside.

Appendix A. Electronic Supplementary Information

Electronic Supplementary Information associated with this paper is available in the online version.

References

1. S. S. Kelkar and T. M. Reineke, *Bioconjugate Chem.*, 2011, **22**, 1879-1903.
2. E. K. Lim, T. Kim, S. Paik, S. Haam, Y. M. Huh and K. Lee, *Chem. Rev.*, 2015, **115**, 327-394.
3. A. M. Smith, M. C. Mancini and S. M. Nie, *Nat. Nanotechnol.*, 2009, **4**, 710-711.
4. R. Philip, A. Penzkofer, W. Bäumler, R. M. Szeimies and C. Abels, *J. Photochem. Photobiol. A Chem.*, 1996, **96**, 137-148.
5. C. Haritoglou, A. Gandorfer, M. Schaumberger, R. Tadayoni, A. Gandorfer and A. Kampik, *Invest. Ophth. Vis. Sci.*, 2003, **44**, 2722-2729.
6. J. V. Frangioni, *Curr. Opin. Chem. Biol.*, 2003, **7**, 626-634.
7. H. J. Lim and C. H. Oh, *Photodiagnosis Photodyn. Ther.*, 2011, **8**, 337-342.
8. E. Smretschnig, S. Ansari-Shahrezaei, S. Hagen, C. Glittenberg, I. Krebs and S. Binder, *Retina-J. Ret. Vit. Dis.*, 2013, **33**, 316-323.
9. V. V. Tuchin, E. A. Genina, A. N. Bashkatov, G. V. Simonenko, O. D. Odoevskaya and G. B. Altshuler, *Laser. Surg. Med.*, 2003, **33**, 296-310.
10. A. Klein, R. M. Szeimies, W. Baumler, F. Zeman, S. Schreml, U. Hohenleutner, M. Landthaler, M. Koller and P. Babilas, *Br. J. Dermatol.*, 2012, **167**, 333-342.
11. S. Yoneya, T. Saito, Y. Komatsu, I. Koyama, K. Takahashi and J. Duvoll-Young, *Invest. Ophth. Vis. Sci.*, 1998, **39**, 1286-1290.
12. C.-M. Ho, A. Dhawan, R. D. Hughes, S. C. Lehec, J. Puppi, C. Philippeos, P.-H. Lee and R. R. Mitry, *Asian J. Surg.*, 2012, **35**, 9-15.

13. M. A. Yaseen, J. Yu, B. S. Jung, M. S. Wong and B. Anvari, *Mol. Pharmaceut.*, 2009, **6**, 1321-1332.
14. B. Bahmani, C. Y. Lytle, A. M. Walker, S. Gupta, V. I. Vullev and B. Anvari, *Int. J. Nanomed.*, 2013, **8**, 1609-1620.
15. S. M. El-Daly, A. M. Gamal-Eldeen, M. A. M. Abo-Zeid, I. H. Borai, H. A. Wafay and A. R. B. Abdel-Ghaffar, *Photodiagnosis Photodyn. Ther.*, 2013, **10**, 173-185.
16. T. Lajunen, L. S. Kontturi, L. Viitala, M. Manna, O. Cramariuc, T. Rog, A. Bunker, T. Laaksonen, T. Viitala, L. Murtomaki and A. Urtti, *Mol. Pharmaceut.*, 2016, **13**, 2095-2107.
17. D. Couto, M. Freitas, G. Porto, M. A. Lopez-Quintela, J. Rivas, P. Freitas, F. Carvalho and E. Fernandes, *Arch. Toxicol.*, 2015, **89**, 1759-1769.
18. B. Bahmani, D. Bacon and B. Anvari, *Sci. Rep.*, 2013, **3**, 2180.
19. J. M. Burns, R. Vankayala, J. T. Mac and B. Anvari, *ACS Appl. Mater. Interfaces*, 2018, **10**, 27621-27630.
20. Q. Pei, X. L. Hu, X. H. Zheng, S. Liu, Y. W. Li, X. B. Jing and Z. G. Xie, *ACS Nano*, 2018, **12**, 1630-1641.
21. G. Y. Wan, B. W. Chen, L. Li, D. Wang, S. R. Shi, T. Zhang, Y. Wang, L. Y. Zhang and Y. S. Wang, *Biomaterials*, 2018, **155**, 25-40.
22. L. Rao, Q. F. Meng, L. L. Bu, B. Cai, Q. Q. Huang, Z. J. Sun, W. F. Zhang, A. Li, S. S. Guo, W. Liu, T. H. Wang and X. Z. Zhao, *ACS Appl. Mater. Interfaces*, 2017, **9**, 2159-2168.
23. J. G. Piao, L. M. Wang, F. Gao, Y. Z. You, Y. J. Xiong and L. H. Yang, *ACS Nano*, 2014, **8**, 10414-10425.
24. J. R. Peng, Q. Yang, W. T. Li, L. W. Tan, Y. Xiao, L. J. Chen, Y. Hao and Z. Y. Qian, *ACS Appl. Mater. Interfaces*, 2017, **9**, 44410-44422.
25. C.-M. J. Hu, L. Zhang, S. Aryal, C. Cheung, R. H. Fang and L. Zhang, *Proc. Natl. Acad. Sci. U.S.A.*, 2011, **108**, 10980-10985.
26. Y. Godfrin, X. Thomas, Y. Bertrand and C. Duget, *Blood*, 2007, **110**, 4325-4325.
27. J. C. Tang, A. Partono and B. Anvari, *IEEE Trans. Biomed. Eng.*, 2018, DOI: 10.1109/TBME.2018.2866368.
28. D. Peer, J. M. Karp, S. Hong, O. C. Farokhzad, R. Margalit and R. Langer, *Nat. Nanotechnol.*, 2007, **2**, 751-760.
29. E. Blanco, H. Shen and M. Ferrari, *Nat. Biotechnol.*, 2015, **33**, 941-951.
30. J. M. Burns, W. Jia, J. S. Nelson, B. Majaron and B. Anvari, *J. Biomed. Opt.*, 2018, **23**, 1-10.
31. B. Ebert, B. Riefke, U. Sukowski and L. C. Kai, *J. Biomed. Opt.*, 2011, **16**, 066003.
32. Y. C. Kuo, H. C. Wu, D. Hoang, W. E. Bentley, W. D. D'Souza and S. R. Raghavan, *Langmuir*, 2016, **32**, 171-179.
33. E. H. Eylar, M. A. Madoff, O. V. Brody and J. L. Oncley, *J. Biol. Chem.*, 1962, **237**, 1992-2000.
34. J. R. Durocher, R. C. Payne and M. E. Conrad, *Blood*, 1975, **45**, 11-20.
35. S. Kwon, C. Davies-Venn and E. M. Sevick-Muraca, *Neurogastroent. Motil.*, 2012, **24**, 494-497.
36. S. Eguchi, M. Takatsuki, K. Yamanouchi, M. Hidaka, A. Soyama, T. Tomonaga, Y. Tajima and T. Kanematsu, *Transplantation*, 2009, **88**, 747-748.
37. E. Koren and V. P. Torchilin, *IUBMB Life*, 2011, **63**, 586-595.
38. S. M. Moghimi, *Adv. Drug Deliver. Rev.*, 1995, **17**, 103-115.
39. R. E. Mebius and G. Kraal, *Nat. Rev. Immunol.*, 2005, **5**, 606-616.
40. I. V. Pivkin, Z. L. Peng, G. E. Karniadakis, P. A. Buffet, M. Dao and S. Suresh, *Proc. Natl. Acad. Sci. U.S.A.*, 2016, **113**, 7804-7809.
41. V. R. Muzykantov, J. C. Murciano, R. P. Taylor, E. N. Atochina and A. Herraez, *Anal. Biochem.*, 1996, **241**, 109-119.
42. C. H. Villa, A. C. Anselmo, S. Mitragotri and V. Muzykantov, *Adv. Drug Deliver. Rev.*, 2016, **106**, 88-103.
43. M. Hagmann, *Science*, 2000, **288**, 1945-1946.
44. P. A. Oldenborg, A. Zheleznyak, Y. F. Fang, C. F. Lagenaur, H. D. Gresham and F. P. Lindberg, *Science*, 2000, **288**, 2051-2054.
45. J. T. Mac, V. Nunez, J. M. Burns, Y. A. Guerrero, V. I. Vullev and B. Anvari, *Biomed. Opt. Express*, 2016, **7**, 1311-1322.
46. J. G. Mohanty, E. Nagababu and J. M. Rifkind, *Front. Physiol.*, 2014, **5**, 84.
47. J. Kim, H. Lee and S. Shin, *J. Cell. Biotech.*, 2015, **1**, 63-79.
48. G. B. Nash and H. J. Meiselman, *Biophys. J.*, 1983, **43**, 63-73.
49. S. Chien, *Annu. Rev. Physiol.*, 1987, **49**, 177-192.
50. D. Bratosin, J. Mazurier, J. P. Tissier, J. Estaquier, J. J. Huart, J. C. Ameisen, D. Aminoff and J. Montreuil, *Biochimie*, 1998, **80**, 173-195.
51. E. Wisse, F. Braet, D. Z. Luo, R. DeZanger, D. Jans, E. Crabbe and A. Vermoesen, *Toxicol. Pathol.*, 1996, **24**, 100-111.
52. Y. N. Zhang, W. Poon, A. J. Tavares, I. D. McGilvray and W. C. W. Chan, *J. Control. Release*, 2016, **240**, 332-348.
53. F. B. Yu, T. Y. Jiang, J. H. Zhang, L. H. Cheng and S. L. Wang, *Pharmazie*, 2007, **62**, 528-533.
54. X. M. Zhang, Q. Zhang, Q. Peng, J. Zhou, L. F. Liao, X. Sun, L. Zhang and T. Gong, *Biomaterials*, 2014, **35**, 6130-6141.
55. D. Y. Gao, T. T. Lin, Y. C. Sung, Y. C. Liu, W. H. Chiang, C. C. Chang, J. Y. Liu and Y. C. Chen, *Biomaterials*, 2015, **67**, 194-203.
56. J. Desilets, A. Lejeune, J. Mercer and C. Gicquaud, *Anticancer Res.*, 2001, **21**, 1741-1747.
57. G. Patel, G. Kher and A. Misra, *J. Drug Target.*, 2012, **20**, 155-165.
58. J. F. Tan, A. Thomas and Y. L. Liu, *Soft Matter*, 2012, **8**, 1934-1946.
59. F. Gentile, A. Curcio, C. Indolfi, M. Ferrari and P. Decuzzi, *J. Nanobiotechnology*, 2008, **6**, 9.
60. M. B. Fish, C. A. Fromen, G. Lopez-Cazares, A. W. Golinski, T. F. Scott, R. Adili, M. Holinstat and O. Eniola-Adefeso, *Biomaterials*, 2017, **124**, 169-179.
61. C. Y. Watson, R. M. Molina, A. Louzada, K. M. Murdaugh, T. C. Donaghey and J. D. Brain, *Int. J. Nanomed.*, 2015, **10**, 4173-4184.
62. P. Bourrinet, H. H. Bengele, B. Bonnemain, A. Dencausse, J. M. Idee, P. M. Jacobs and J. M. Lewis, *Invest. Radiol.*, 2006, **41**, 313-324.
63. M. A. Suckow, P. Danneman and C. Brayton, *The laboratory mouse*, CRC Press, Boca Raton, Fla., 2001.
64. L. M. Serfilippi, D. R. Pallman and B. Russell, *Contemp. Top. Lab Anim. Sci.*, 2003, **42**, 46-52.
65. M. V. Marshall, D. Draney, E. M. Sevick-Muraca and D. M. Olive, *Mol. Imaging Biol.*, 2010, **12**, 583-594.
66. J. Shi, G. E. Gilbert, Y. Kokubo and T. Ohashi, *Blood*, 2001, **98**, 1226-1230.
67. A. Hochreiter-Hufford and K. S. Ravichandran, *Cold Spring Harb. Perspect. Biol.*, 2013, **5**, a008748.

68. N. Lu and Z. Zhou, *Int. Rev. Cell Mol. Biol.*, 2012, **293**, 269-309.
69. J. W. Semple, J. E. Italiano, Jr. and J. Freedman, *Nat. Rev. Immunol.*, 2011, **11**, 264-274.
70. P. F. Lalor, J. Herbert, R. Bicknell and D. H. Adams, *Am. J. Physiol. Gastrointest. Liver Physiol.*, 2013, **304**, G469-478.
71. A. Radomski, P. Jurasz, D. Alonso-Escolano, M. Drews, M. Morandi, T. Malinski and M. W. Radomski, *Br. J. Pharmacol.*, 2009, **146**, 882-893.
72. S.-H. Yun, E.-H. Sim, R.-Y. Goh, J.-I. Park and J.-Y. Han, *Biomed Res. Int.*, 2016, **2016**, 9060143.
73. K. E. O'Connell, A. M. Mikkola, A. M. Stepanek, A. Vernet, C. D. Hall, C. C. Sun, E. Yildirim, J. F. Staropoli, J. T. Lee and D. E. Brown, *Comp. Med.*, 2015, **65**, 96-113.

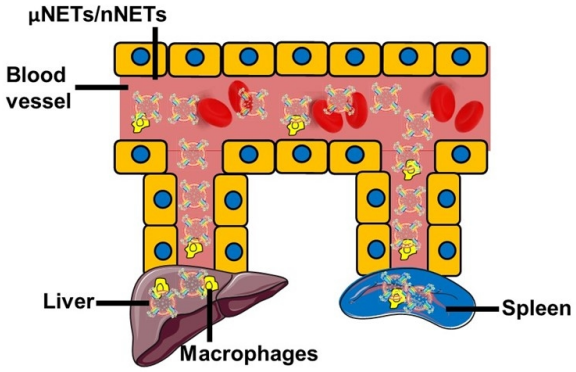

338x190mm (96 x 96 DPI)